



Antibacterial ability of black titania in dark: Via oxygen vacancies mediated electron transfer



Zhe Li ^{a,b,1}, Engui Wang ^{b,c,1}, Yingzi Zhang ^{d,1}, Ruizeng Luo ^{b,c}, Yansong Gai ^b, Han Ouyang ^c, Yulin Deng ^e, Xiaozhong Zhou ^{d,*}, Zhou Li ^{b,c,**}, Hongqing Feng ^{b,c,**}

^a Institute of Engineering Medicine, Beijing Institute of Technology, Beijing 100081, China

^b Beijing Institute of Nanoenergy and Nanosystems, Chinese Academy of Sciences, Beijing 101400, China

^c School of Nanoscience and Technology, University of Chinese Academy of Sciences, Beijing 100049, China

^d Department of Orthopedics, the Second Affiliated Hospital of Soochow University, No. 1055, Sanxiang Road, Gusu District, Suzhou 215004, Jiangsu, China

^e School of Life, Beijing Institute of Technology, Beijing 100081, China

ARTICLE INFO

Article history:

Received 8 February 2023

Received in revised form 9 March 2023

Accepted 11 March 2023

Available online xxxx

Keywords:

Black titania

Oxygen vacancies

Antibacterial activity

Electron transfer

Ti implant

ABSTRACT

Antibacterial ability is greatly demanded for biomedical implants to prevent after-surgery infections. Titania is the oxidative layer of the widely used Ti implants, and is well known to gain antibacterial ability via photocatalysis. However, to prevent the implant related infections, antibacterial ability in dark is required. In this work, we carry out a study on the in-dark antibacterial ability of black titania nanotube arrays (B-TNT) on Ti substrate, and the mechanisms are also deeply investigated. We discover that B-TNT have prominent bactericidal ability in dark, and the mechanisms lie on the electron transfer mediated by the oxygen vacancies (V_o) of B-TNT. With single-electron trapped in their sites, the V_o function as both electron donors and acceptors, generating superoxide anions, hydroxyl radicals and singlet oxygen to do bacteria killing. Moreover, the V_o have the ability to trigger unusual extracellular electron transfer (EET) from the bacteria on B-TNT, which eventually leads to bacteria death. The generation of the Reactive Oxygen Species (ROS) and the force EET mediated by V_o work together to enable the antibacterial ability of B-TNT in dark.

© 2023 Elsevier Ltd. All rights reserved.

Introduction

The demand for orthopedic implants to restore bone loss or function is growing globally due to the aging population [1–4]. Despite of the development of various biomaterials, orthopedic implant associated infection is one of the major causes of implant failure [5–7]. Titanium (Ti) as the most widely applied metal orthopedic materials, has an infection rate of more than 10 % after surgery [8]. The infections often require extensive surgical intervention and long-term antibiotic therapy. In addition to causing pains and financial losses, severe infections can even lead to amputation or life-threatening sepsis [9–12].

Although titania (TiO_2) as the intrinsic oxidative layer of Ti can gain antibacterial ability via photocatalysis [13–18], the requirement of light irradiation makes it unapplicable for biomedical implants. Luckily, in recent years a new concept of antibacterial theory based on electron transfer has been proposed [19–22]. Electron transfer is not only a common event in photochemical modulation, but also a basic process for energy generation in organisms [23,24]. Therefore, material surface and microorganisms may have interactions via electron transfer, leading to bacteria inactivation eventually. Cao et al. found that on Ag doped TiO_2 surface, electrons were stored in the Ag nanoparticles, and induced valence-band hole accumulation which caused cytosolic content leakage of the bacteria [25]. Panda et al. reported that graphene oxide (GO) coatings can achieve superior antibacterial properties when attached to certain substrates, and the anti-bacterial ratio is closely related to the conductivity of the substrates [26]. A study by Wu's group showed that hydroxyapatite and molybdenum disulfide (HA/MoS₂) coating on Ti can trigger electron transfer between bacteria and the implant, preventing in vivo infection [27]. This new anti-bacteria theory based on electron transfer brings in a different perspective for developing

* Corresponding author.

** Corresponding authors at: Beijing Institute of Nanoenergy and Nanosystems, Chinese Academy of Sciences, Beijing 101400, China.

E-mail addresses: zhouxz@suda.edu.cn (X. Zhou), zli@binn.cas.cn (Z. Li), fenghongqing@binn.cas.cn (H. Feng).

¹ Zhe Li, E. Wang and Y. Zhang contribute equally to this work.

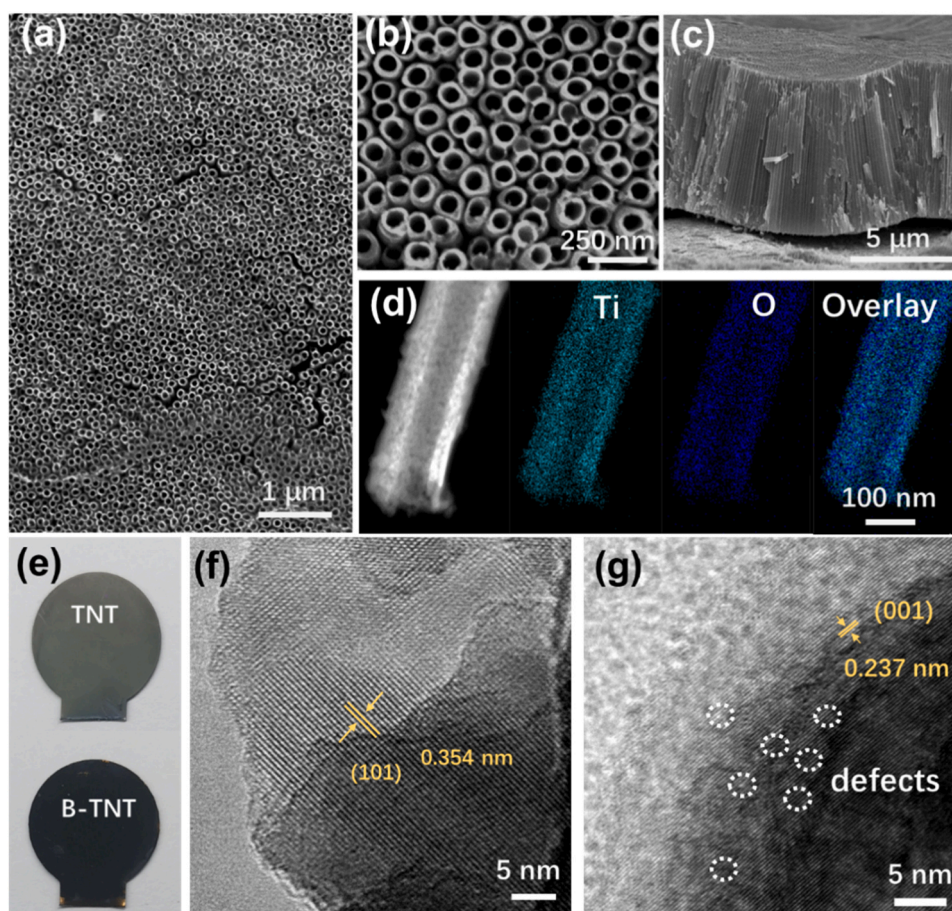


Fig. 1. The fabricated TNT and B-TNT. (a-c) SEM image of TNT; (d) STEM-EELS images of Ti and O elements; (e) photo of TNT and B-TNT; (f-g) HRTEM of TNT and B-TNT.

infection-prevention implants, and the understanding toward this concept is just beginning.

Apart from electron transfer induced by the combination of top layer and the substrate, defects in materials can also play the role of facilitating electron transfer [28]. Shi et al. reported an anti-biofilm strategy by introducing nanoholes in MoS_2 nanosheets as active electron donor, to boost electron transport and biofilm inactivation [29]. Li et al. demonstrated that sulfur vacancies in the quantum dots of transition metal dihalides can ensure one-way electron transfer from the external environment to the quantum dots, leading to reactive oxygen species (ROS) free sterilization [30]. Wang et al. synthesized defects-rich MoS_2/rGO vertical heterostructures (VHS), and demonstrated that the VHS had defects and irradiation dual-enhanced triple enzyme-like activities for promoting ROS generation and bacterial inactivation [31].

Although the above works have achieved efficient bacteria killing together with many interesting findings, there still gaps to fulfill the demand for antibacterial implants. One is that most of the studies are conducted with nanomaterials, not implant surface. Second, many of them didn't get rid of the dependence on photocatalysis, which still has limitations for applications inside bodies. Moreover, the detailed information of the interactions between the bacteria and the materials still needs further disclosure.

In order to endow Ti implants with bactericidal ability in dark, we look into ways to generate defects in titania, and find the so-called black titania. By doing TiO_2 annealing under vacuum or in a reducing atmosphere, black titania with oxygen vacancies (Vo) and/or Ti^{3+} defects can be constructed. In recent years, black titania has attracted extensive research interest in the physical and chemical fields, because they have excellent light harvesting capabilities and

photocatalytic properties [32–34]. However, the antibacterial ability of black titania in dark has never been considered up until now. In this work, we fabricate a layer of black titania nanotube array (B-TNT) on Ti substrate, and the antibacterial ability and mechanisms of the B-TNT samples is thoroughly studied. We discover that B-TNT has prominent bactericidal ability in dark, and the mechanisms lie on Vo only. Vo act as both electron donor and acceptor, generating superoxide anion $\cdot\text{O}_2^-$, hydroxyl radical $\cdot\text{OH}$, and singlet oxygen $^1\text{O}_2$ on the sample surface which have strong killing over the bacteria. Moreover, Vo have triggered extracellular electron transfer (EET) in the bacteria on B-TNT, which doesn't happen in their normal life activity. The generation of ROS and the triggered EET via Vo work together, and endow B-TNT with antibacterial ability in dark.

Results and discussion

Sample characterizations

The B-TNT is fabricated on the basis of normal titania nanotube array (TNT). As shown in Fig. 1a, a large area of uniform and dense nanotube array is formed on the Ti substrate (Fig. 1a). The nanotube diameter is about 100 nm, and the tube length is about 7 μm (Fig. 1b-c). Scanning transmission electron microscopy (STEM) and electron energy loss spectroscopy (EELS) shows that Ti and O elements are uniformly distributed in the entire tube wall (Fig. 1d). To make B-TNT samples, the anodized TNT is annealed in N_2 , while normal TNT is annealed in air. After annealing in N_2 , B-TNT turns out a black color, and normal TNT shows a color of white grey (Fig. 1e). High resolution TEM (HRTEM) images of TNT and B-TNT are shown in Fig. 1f-g. The interplanar spacing of 0.354 nm and 0.237 nm indicate the (101) and

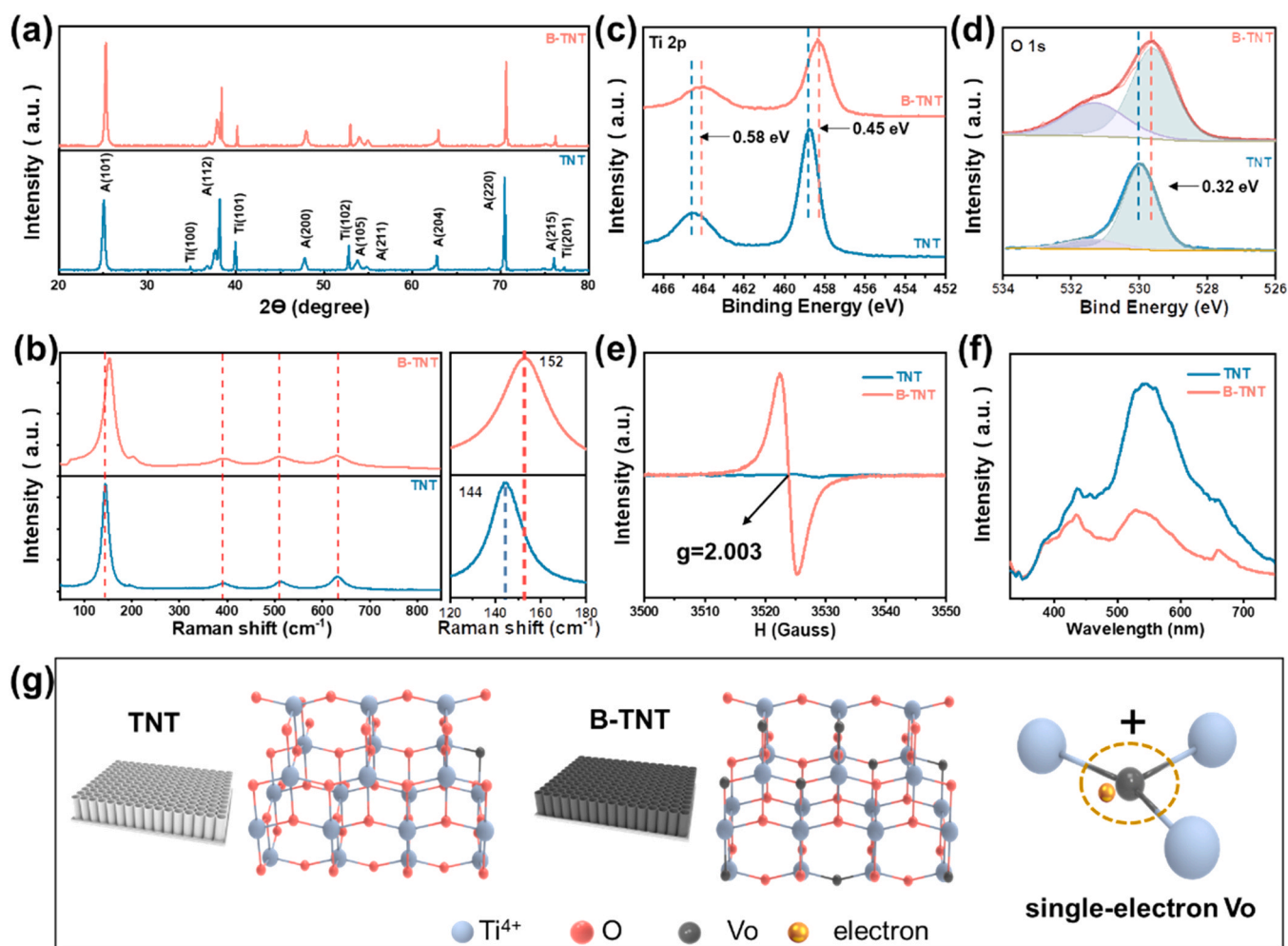


Fig. 2. Characterization of TNT and B-TNT: (a) XRD patterns; (b) Raman spectrometry; (c-d) XPS HR spectra of Ti 2p and O 1s; (e) EPR signal of the single-electron trapped Vo; (f) PL spectra. (g) the atomic model of TNT, B-TNT and the single-electron trapped Vo.

(001) facet of anatase TiO_2 respectively. Defects are observed in the B-TNT sample (Fig. 1g). As shown in Figure S1, the bandgap of B-TNT is narrowed to 2.42 eV compared to that of 3.12 eV of TNT.

More characterizations are carried out to identify various properties of B-TNT. X-ray diffraction (XRD) spectra of TNT and B-TNT show almost identical peak alignment, displaying dominant diffraction peaks at $2\theta = 25.3^\circ$ (101), 38.4° (112), and 70.3° (220) for both TNT and B-TNT (Fig. 2a). These indicate the formation of anatase titanium dioxide. The peaks of Ti (101), Ti (102) and Ti (201) indicate the Ti substrate beneath. The anatase phases of TNT and B-TNT are further confirmed by Raman spectroscopy, as shown in Fig. 2b. The major Raman bands of the anatase phase are presented by the peaks at around 147.7 cm^{-1} for Eg (1), 200.4 cm^{-1} for Eg (2), 394.9 cm^{-1} for B1g (1), 516.9 cm^{-1} for B1g (2) + A1g (1), and 636.5 cm^{-1} for Eg (3), respectively. The main Eg (1) peak shifts obviously toward higher wavenumber from 143.7 cm^{-1} to 152.4 cm^{-1} , which is attributed to the Vo formation required to maintain charge neutrality in the anatase TiO_2 lattice [35]. The chemical states of the Ti and O elements are characterized by X-ray photoelectron spectroscopy (XPS). In the XPS Ti 2p high resolution spectrum of TNT, two peaks at 458.78 and 464.53 eV are assigned to Ti^{4+} [36]; and they respectively shifted by 0.58 and 0.45 eV toward lower binding energy in the B-TNT spectra (Fig. 2c), which suggest that B-TNT has a higher electron density [37]. Both TNT and B-TNT have no obvious

Ti^{3+} peaks, suggesting that the amount of Ti^{3+} is very low for both samples. In the O1s spectra, the peak of lattice O (Lo) also shifted toward low binding energy by 0.32 eV from 530.03 to 529.71 eV for B-TNT (Fig. 2d). Apart from this, an apparent shoulder peak turns out in B-TNT spectrum locating at 531.33 eV, which can be assigned to Vo [38]. The deconvolution of the O1s peak indicate that the ratio of Vo: Lo is 0.51 for B-TNT, and 0.17 for TNT, suggesting that a large amount of Vo is generated in B-TNT. Meanwhile, Electron Paramagnetic Resonance (EPR) is employed to evaluate the Vo and Ti^{3+} formation in B-TNT (Fig. 2e). The B-TNT sample exhibits a strong signal of Vo, but no sign of Ti^{3+} , which is consistent with the results of XPS. Because EPR can only detect the signals of unpaired electrons, the Vo in our B-TNT sample are identified to be single-electron trapped Vo [36,39]. The photoluminescence (PL) spectra show that the intensity of peaks in B-TNT is significantly lower than that in TNT in the range of 330–750 nm (Fig. 2f). This indicates that B-TNT has enabled faster electron-hole separation and migration after the 325 nm laser irradiation in the PL equipment, resulting in lower carrier recombination and lower PL signal intensity. The peaks around 430 nm become dominate in the B-TNT spectrum, which is believed to be contributed by Vo [40,41]. Taken the above results together, we conclude that in this study, we obtain B-TNT with single-electron accompanied Vo as the defect contributor, without detectable involvement of Ti^{3+} . The atomic model of B-TNT is shown in Fig. 2g.

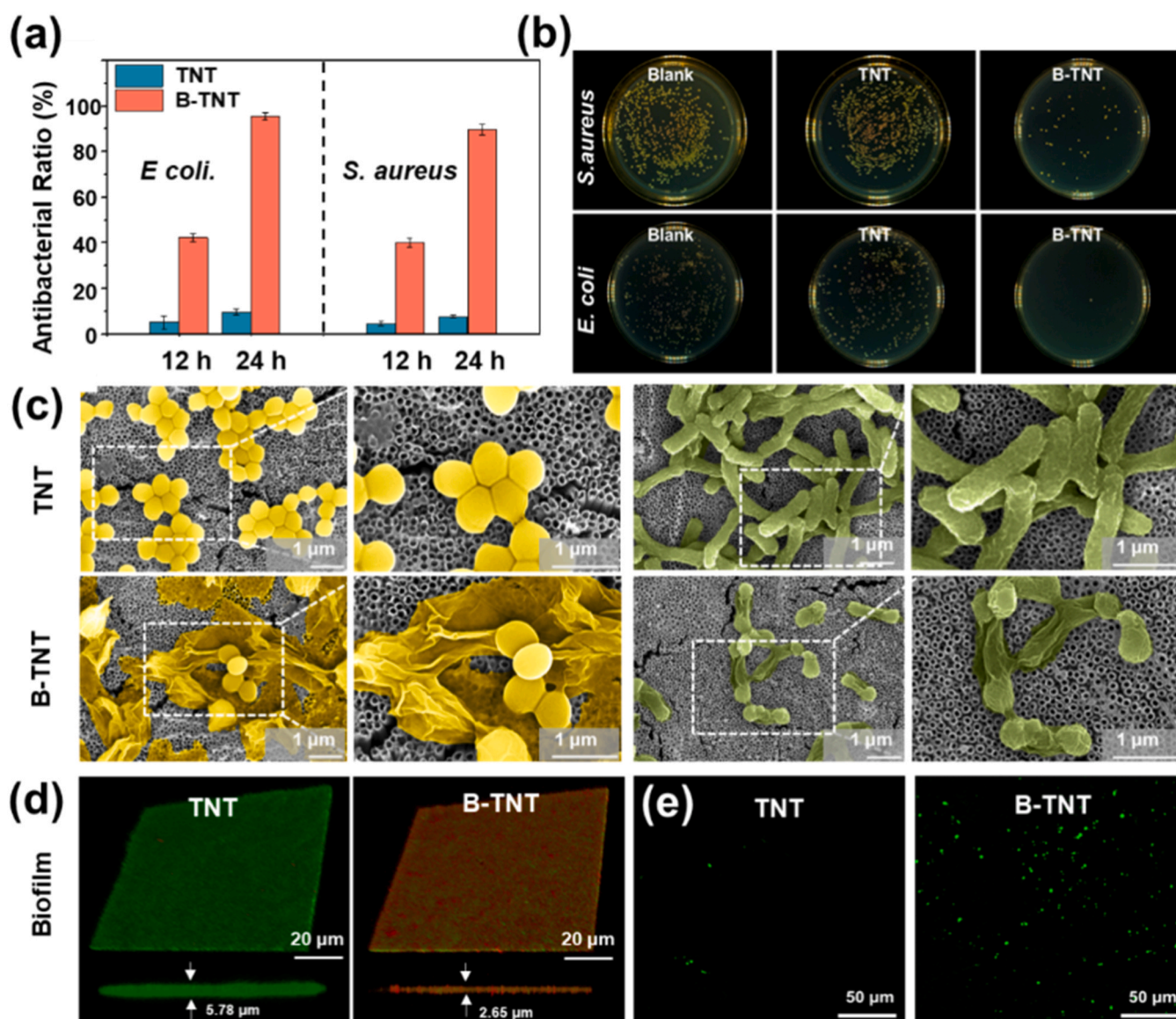


Fig. 3. The evaluation of the anti-bacteria ability of B-TNT in dark. (a) Bacteria killing ratio of TNT and B-TNT. (b) The photos of CFU plating of *E. coli* and *S. aureus* after treated with TNT and B-TNT. (c) SEM images of *S. aureus* (yellow) and *E. coli* (green) on TNT and B-TNT. (d) Live-Dead fluorescent staining for the anti-biofilm performance of TNT and B-TNT. (e) Intracellular ROS staining of *S. aureus* on TNT and B-TNT.

Antibacterial ability of B-TNT in dark

The antibacterial property of TNT and B-TNT in dark are studied using typical infection bacteria *Staphylococcus aureus* (*S. aureus*) and *Escherichia coli* (*E. coli*). As shown in Fig. 3a, after culturing on B-TNT for 12 h, the killing efficiency of *E. coli* and *S. aureus* is 42.3 % and 39.8 %, respectively; after 24 h, the inactivation ratio increased to 95.7 % for *E. coli* and 90.2 % for *S. aureus*. Typical photos of the bacteria CFU plating are shown in Fig. 3b. SEM is used to observe the morphology of bacteria growing on TNT and B-TNT as shown in Fig. 3c. The density of bacteria on B-TNT is significantly lower than that in on TNT, for both *E. coli* (green) and *S. aureus* (yellow). The bacteria on TNT are doing normal proliferation and division, while those on B-TNT are having difficulty doing division. Moreover, many bacteria on B-TNT completely collapse displaying very abnormal cell shapes. In addition, the long-term anti-biofilm performance of TNT and B-TNT samples after 48 h culture is evaluated (Fig. 3d). The Live-Dead fluorescence staining shows that biofilm has formed on both TNT and B-TNT, but the biofilm on B-TNT is much thinner, with a thickness of 2.65 μm , less than half of that on TNT (5.78 μm). More

importantly, the biofilm on B-TNT show very small, discrete bacterial colonies, and many of them are red, indicating that the bacteria have been killed. The bacteria on TNT and B-TNT are further examined for oxidative stress. The group of *S. aureus* cells on B-TNT display strong green fluorescence suggesting high level of intracellular ROS, but only a few cells are stained green on TNT (Fig. 3e). In addition, the antibacterial behavior of the newly prepared B-TNT (B-TNT) is compared with those that have been placed in ambient air for two weeks (B-TNT-OLD) (Figs. S2–4). The B-TNT and B-TNT-OLD have the same appearance and color (Figure S2), and the antibacterial ratios show no significant difference between the two groups (Figs. S3–4). These results prove that B-TNT have very stable antibacterial ability.

Antibacterial mechanisms of B-TNT in dark

Since strong intracellular ROS are detected in the bacteria on B-TNT, the origin of the ROS is studied. First, the instinct ability of B-TNT to generate ROS in dark is studied by EPR. The EPR signals of $\bullet\text{O}_2^-$, $\bullet\text{OH}$, and $^1\text{O}_2$ radicals are examined using DMPO-CH₄O, DMPO-H₂O and TEMP-CH₄O spin trap reagents, respectively. $\bullet\text{O}_2^-$, $\bullet\text{OH}$, and

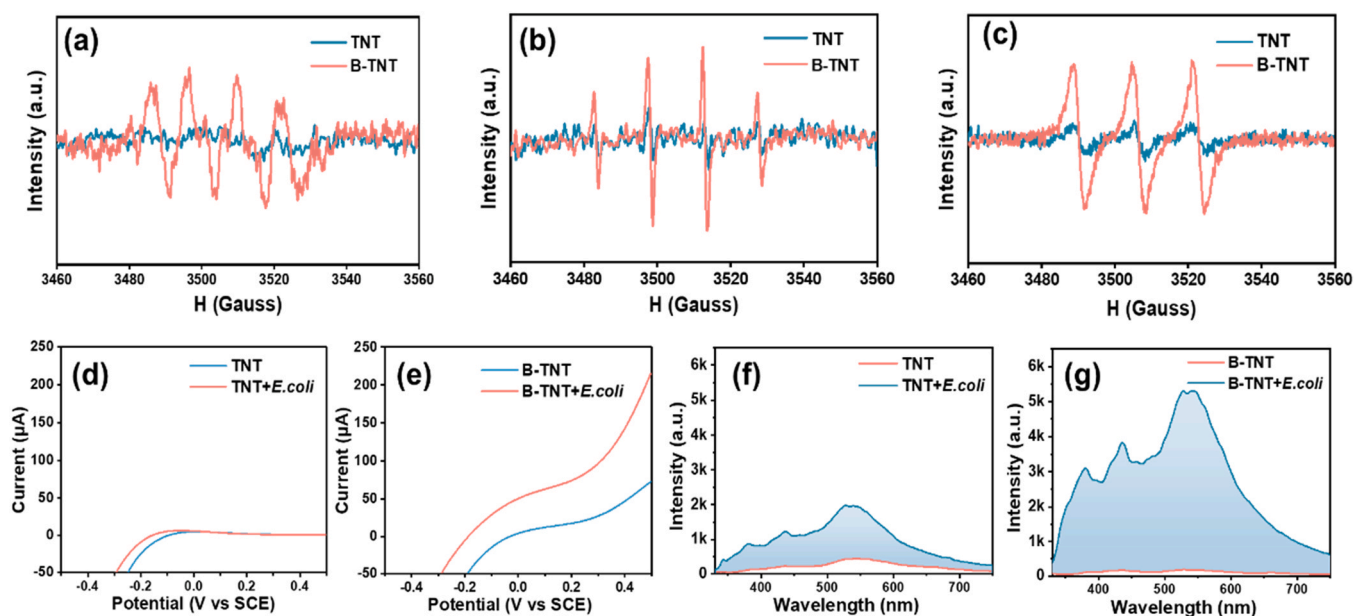


Fig. 4. Mechanism study of the antibacterial property of B-TNT in dark. (a-c) EPR detection of ROS generation on B-TNT in dark. (d-e) EET from the bacteria to B-TNT detected by the I-V curves. (f-g) EET from the bacteria to B-TNT detected using the PL survey.

$^1\text{O}_2$ radicals are successfully detected on B-TNT in dark without light irradiation (Fig. 4a–c). The typical generation of $\cdot\text{O}_2^-$ is by an electron donor to give one electron to O_2 , and the typical generation of $\cdot\text{OH}$ is by an electron acceptor to extract one electron out of H_2O leaving H^+ and $\cdot\text{OH}$ [42,43]. Because we have identified that the Vo in our B-TNT are single-electron trapped, they act as both electron donors and acceptors to enable the reactions as follows (Reaction 1–2). The typical generation of $^1\text{O}_2$ is caused by the reaction between $\cdot\text{O}_2^-$ and h^+ [44,45]. As shown in Fig. 4c, $^1\text{O}_2$ is also generated in B-TNT. This suggests that Vo acting as electron acceptors may play the role of h^+ to generate $^1\text{O}_2$ by reacting with $\cdot\text{O}_2^-$ (Reaction 3). These results demonstrate that single-electron trapped Vo have the ability to generate $\cdot\text{O}_2^-$, $\cdot\text{OH}$, and $^1\text{O}_2$ spontaneously without the need of light.



Next, we conduct more experiment to disclose whether B-TNT can have interaction with the bacteria via electron transfer mediated by the single-electron trapped Vo . Bacteria current is measured in a similar setup with that of light current measurement, but bacteria are introduced to the system instead of light. After attaching a layer of *E. coli* film on B-TNT, the current-potential (I-V) curve is elevated largely compared to bare B-TNT: with a potential of 0.5 V, the current is increased from 50 μA to 200 μA (Fig. 4e). This indicates that the bacteria film undergoes extracellular electron transfer (EET) serving as electron donors to the Vo , which increases the current. The I-V curves of TNT have no such pattern. The curve of normal TNT is nearly zero, and adding bacteria barely changes the curve (Fig. 4d).

To verify the EET from bacteria to B-TNT, PL survey is carried out with *E. coli* on the surface of TNT and B-TNT (Fig. 4f-g). The PL intensity of both TNT and B-TNT increase after adding the *E. coli* film. This means that the recombination of electrons and holes increase, suggesting that bacteria transfer electrons to the substrate which results in more charge recombination and more illuminance. TNT+*E. coli* shows higher PL signal than bare TNT (from 600 to 2000), which can be regarded as the basic increase caused by the bacteria. The increase of PL signal of B-TNT+*E. coli* is much larger (from 250 to

5500), almost three folds of that of TNT. The additional increase of the PL signal is caused by the interaction between Vo and the bacteria. This result confirms the dominate ability of B-TNT to induce bacteria electron outflow.

The overall anti-bacteria mechanism is illustrated in Fig. 5. We obtain B-TNT containing single-electron trapped Vo as the defect contributor. The antibacterial activity of B-TNT in dark is enabled from two aspects. First, when in contact with water and oxygen, the B-TNT produces hydroxyl radicals, superoxide anions and singlet oxygen due to the both electron acceptor and donor ability of Vo , and the ROS play the role of sterilization. Second, the electron acceptor tendency of Vo can attract active electrons in the bacterial respiratory chain, forming EET (yellow arrow) from bacteria to B-TNT. The normal electron transfer pathway in *E. coli* is indicated with dashed green arrows in the figure, which has highly ordered temporal and spatial sequences [46]. In normal conditions, EET does not take place for the infection related bacteria such as *E. coli* and *S. aureus* [47]. The unusual EET from the bacteria to B-TNT eventually leads to their death.

In depth discussion on Vo mediated antibacterial activity in dark

After we finish this study, a look back survey reveals that just recently, two groups have reported antibacterial activity in dark mediated by Vo . Gao et al. developed Vo rich $\alpha\text{-MoO}_3$ bactericidal nanocatalysts in dark and described a surface-dependent mechanism of ROS generation for antibacterial activity [48]. Also, Liu et al. found that Ag-modified ZnO nanorods had better antibacterial effects on clinical drug-resistant bacteria because the modified ZnO can produce H_2O_2 , which is highly related to the Vo concentration [49]. These works together with ours have made a success step toward the light-independent electron-transfer based disinfection. Nevertheless, the three works have distinct differences. Gao's and Liu's work are based on 1D nanoparticles, while ours are based on 2D nanotube arrays. Gao et al. found that Vo in dark can induce the generation of superoxide and Liu et al. found that Vo in dark can induce the generation of H_2O_2 . Only one type of ROS was detected in the nanoparticles and nanorods each, while in the B-TNT, we have detected three types of ROS. The less rich ROS generation in the nanoparticles and nanorods may lie in the fact that they as 1D

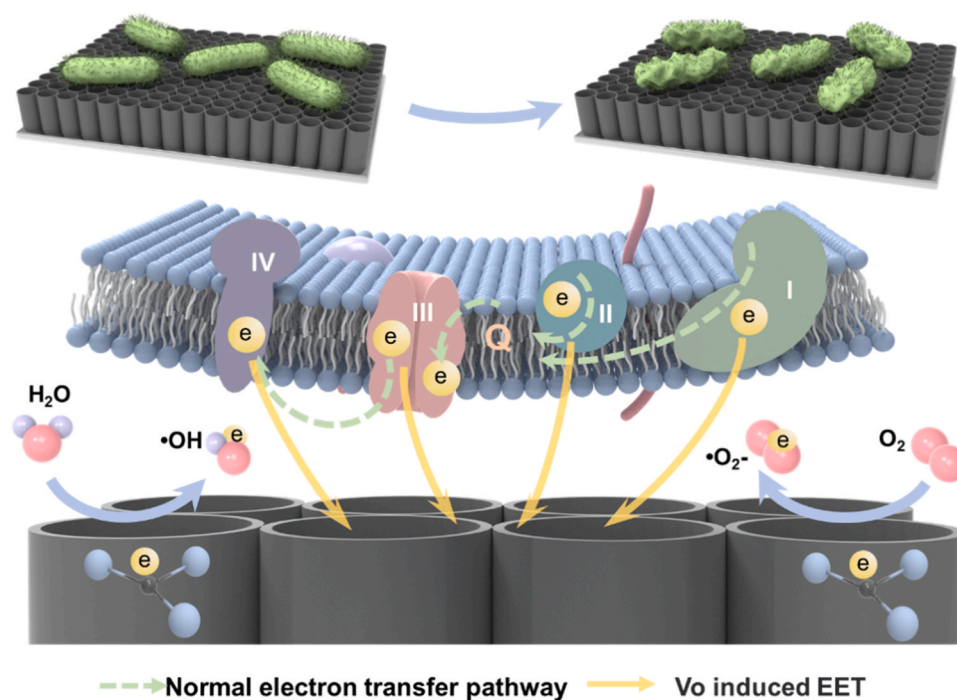


Fig. 5. Illustration of the antibacterial mechanism of B-TNT in dark.

materials have smaller specific surface area (SSA) than the 2D nanotube array [50,51]. A smaller SSA reduces the possibility for O_2 and H_2O to react with the Vo and the possibility of ROS generation. Therefore, if fabricating black TiO_2 nanoparticle, they should have certain ROS generation ability just like the B-TNT, but with a lower efficiency, because the black TiO_2 nanoparticle have smaller SSA. But they may have advantages when applied in other scenarios, for example, water pollution treatment. In addition, our work verifies that EET has been triggered from the bacteria to the B-TNT, which is abnormal for those infection related bacteria and finally leads to their death. However, EET is not likely to be induced by the nanoparticles, because the nanoparticles, diffused in solution and taken in by the bacteria, are not able to induce oriented electron transfer or current. The forced EET triggered by Vo is another critical bactericidal mechanism associated with B-TNT. This is the most important superiority of our work over the published ones.

Conclusion

In summary, we have constructed black titania nanotube arrays (B-TNT) on Ti surface containing single-electron trapped Vo as the defect source, without the involvement of Ti^{3+} . The B-TNT has the universal properties as the previously reported black titania, including the absorption of visible light and the narrowing of the band gap. More importantly, we have discovered that B-TNT has antibacterial properties in dark, without the requirement of light. The antibacterial mechanisms of B-TNT in dark are as follows. On one hand, single-electron trapped Vo has the ability to both gain and lose electrons. With the presence of water and oxygen, hydroxyl radical, superoxide anion radical and singlet oxygen are generated, and the bacteria are killed by these ROS. On the other hand, the Vo can capture the active electrons in the bacterial respiratory chain, and the bacteria die from this forced EET. The abnormal EET is confirmed in our study by both EIS and PL survey. To the best of our knowledge, this study is the first one to identify B-TNT with antibacterial ability in dark and discover the abnormal EET triggered by Vo . With the antibacterial property in dark, as well as the simple preparation process without the introduction of foreign substances, B-TNT is a

promising new candidate for the infection prevention interface of titanium implants.

Materials and methods

Fabrication of B-TNT

Black titania nanotube arrays are prepared by electrochemical anodizing of titanium sheets in NH_4F -glycol solution, and annealing of the anodized titania nanotubes in argon. The 14 mm diameter titanium samples with thickness of 1 mm are polished with acid lotion (40 % nitric acid, 10 % hydrofluoric acid, 50 % deionized water) for 3 min. Then, they ultrasonic cleaned with acetone, alcohol and deionized water for 30 min, respectively. After dried with nitrogen, they are cleaned with PLASMA for 3 min. Positive photoresist (S1813) is dripped onto the cleaned titanium samples, rotated for 10 s at 1000 RPM and 30 s at 8000 RPM in a spin coating machine, and dried for 10 min at 80 °C on a hot plate. Anodization is performed in ice bath with a DC power supply (MCH-K1505D, China) at 60 V for 55 min. A graphite electrode and the titanium samples are used as the cathode and anode respectively, with a space of 1 cm. The electrolyte contains 0.55 % ammonium fluoride, 5 % deionized water, 5 % methyl alcohol and 90 % mL glycol. The prepared samples are soaked in acetone, alcohol and deionized water for 1 h sequentially, and dried in the oven at 60 °C. Finally, sample annealing is carried out in the nitrogen atmosphere in the tube furnace, with heating rate of 5 °C/ min, heating temperature of 450 °C and holding time of 3 h, and then cooled naturally in the furnace.

Characterizations of B-TNT

The morphology of TNT is characterized by scanning electron microscopy (SEM, SU8020) and transmission electron microscopy (TEM, Tecnai G2 F20 S-TWIN TMP). The crystallinity of the samples is determined by XRD (PANalytical X 'Pert) and irradiation by $Cu K\alpha$ ($\lambda = 1.54184 \text{ \AA}$) at 30 kV and 10 mA. The UV-visible diffuse reflection spectrum is obtained by Shimadzu UV3600 at room temperature, and the wavelength range is 300–700 nm. The chemical state is

determined by XPS (Thermo Scientific ESCALab 250Xi) with a radiation of 200 W monochromatic Al K α ($h\nu=1486.6$ eV). The foundation pressure in the analysis chamber is about 3×10^{-9} mbar. Electron Paramagnetic Resonance (EPR) spectra are recorded using a spectrometer at room temperature in ambient air (Bruker E500). The chemical structure, crystallinity and molecular interactions are characterized by Raman spectroscopy equipped with an Ar laser (LabRAM HR Evolution, Horiba). The material defects and electron-hole recombination efficiency are analyzed by photoluminescence spectroscopy (PL) equipped with He-Cd lasers operating at 325 nm (LabRAM HR Evolution, Horiba).

Antibacterial analyses

The antibacterial activity of the sterilized samples is assessed with Gram-positive (*S. aureus*, 29213) and Gram-negative (*E. coli*, ATCC 25922) bacteria. In brief, the pure bacteria in LB are cultivated overnight in a rotating shaker at 37 °C, 1:10 diluted and then cultivated to a concentration of $2-3 \times 10^9$ CFU mL $^{-1}$ ($OD_{450} = 0.3$ for *S. aureus* and $OD_{450} = 1.0$ for *E. coli*). The bacteria solution with a concentration of $2-3 \times 10^5$ mL $^{-1}$ is prepared for the antibacterial test. TNT and B-TNT samples are sterilized by soaking in 75 % ethanol for 30 min, repeatedly cleaned with deionized water and dried with nitrogen. 100 μ L bacteria solution is placed on the samples each. After 12 h and 24 h, the bacteria are diluted and plated on agar for CFU analysis to determine the antibacterial effect.

Morphology of bacteria

The bacteria solution is placed on the TNT and B-TNT samples for 24 h. The samples with adhered bacteria are immersed in 2.5 % glutaraldehyde overnight and treated with gradient alcohol (50 %, 60 %, 70 %, 80 %, 90 % and 100 %) for 30 min each for dehydration before they are dried in vacuum. The samples are then put on a specimen stage prior to SEM observation.

Fluorescent staining of bacteria

Bacterial biofilms are formed by continuous culture *S. aureus* for 48 h on the samples. Then the biofilm is stained with the LIVE/DEAD[®]BacLight[™] Bacterial viability kit (Molecular Probes, Inc., Eugene, OR) to assess viability. In short, live bacteria are dyed green and dead bacteria are dyed red. 15 min after staining, the samples are washed with PBS to remove the excess dye, and then placed on a slide under a confocal fluorescence microscope (Leica SP8). The excitation wavelength of green fluorescence is 488/520 nm and that of red fluorescence is 488/630 nm.

Intracellular ROS staining

The intracellular ROS levels are determined by the fluorescent probe, 2',7'-dichlorodihydrofluorescein diacetate (DCFH-DA, Beyotime, China) which could be deacetylated and oxidized to fluorescent products after crossing the membrane of live bacteria. The bacteria are treated with TNT and B-TNT samples for 180 min before 400 μ L of DCFH-DA are spread on the sample surface with protection from light for 15 min. The excess dye is removed by PBS and the samples are put on the sample stage under an inverted fluorescent microscope with 488 nm as the excitation wavelength and 520 nm as the emission wavelength.

Bacteria current detection

The current-potential (I-V) curves are acquired from the samples on an electrochemical workstation (CHI660E, Chenhua, China) with K $_3$ [Fe(CN) $_6$] (5 mM) as the redox system. The TNT or B-TNT samples

serve as the working electrode and a platinum plate and saturated calomel electrode (SCE) as the counter electrode and reference electrode, respectively. The working electrode potential is set between -0.5 and 0.5 V. The samples tested included: TNT, B-TNT, TNT+ *E. coli*, B-TNT+ live *E. coli*; no light is applied to the system. For samples with living *E. coli* on the surface, 100 μ L of the bacteria solution (1×10^8 CFU mL $^{-1}$) is dropped onto the sample surface and dried at 37 °C for 0.5 h to form the bacteria film. Subsequently, the I-V curves of samples with live *E. coli* are acquired.

PL spectrum of bacteria

The material defects and electron-hole recombination efficiency of interface between TNT and bacteria are analyzed by photoluminescence spectroscopy (PL) equipped with He-Cd lasers operating at 325 nm (LabRAM HR Evolution, Horiba). The samples tested included: TNT, B-TNT, TNT+ live *E. coli*, B-TNT+ live *E. coli*. To get samples with living *E. coli* on the surface, 100 μ L of the bacteria solution (1×10^8 CFU mL $^{-1}$) is dropped onto the sample surface and dried at 37 °C for 0.5 h to form the bacteria film. Then, the PL spectrum of bacteria is studied.

CRediT authorship contribution statement

H.Q. Feng designed the research. Zhe Li and E.G. Wang collected the data. Zhe Li, E.G. Wang and Y.Z. Zhang processed the data. R.Z. Luo and Y.S. Gai draw and beautify data images. Zhe Li and H.Q. Feng wrote the original manuscript. O. Han and Y.L. Deng provided suggestions and improved the manuscript. X.Z. Zhou and Zhou Li provided resources and supervision. Zhe Li, Y.Z. Zhang, O. Han, X.Z. Zhou, H.Q. Feng and Zhou Li got fundings. All authors have read and agreed to publish the manuscript.

Data Availability

Data will be made available on request.

Declaration of Competing Interest

The authors declare that they have no known competing financial interests or personal relationships that could have appeared to influence the work reported in this paper.

Acknowledgment

This work was financially supported by the National Natural Science Foundation of China (81971770, T2125003 and 82202348), the Fundamental Research Funds for the Central Universities (E2E46806, E0EG6802X2), Beijing Natural Science Foundation (JQ20038, L212010 and 7224368), China Postdoctoral Science Foundation (2022T150052), Special project of "Technological Innovation" Project of CNNC Medical Industry Co. Ltd (ZHYLYB2021005), Tang Scholar Project of Soochow University and Gusu Health Talent Plan (2022)161.

Appendix A. Supporting information

Supplementary data associated with this article can be found in the online version at [doi:10.1016/j.nantod.2023.101826](https://doi.org/10.1016/j.nantod.2023.101826).

References

- [1] K. Chae, W.Y. Jang, K. Park, J. Lee, H. Kim, K. Lee, C.K. Lee, Y. Lee, S.H. Lee, J. Seo, *Sci. Adv.* 6 (2020) eabb0025.
- [2] Y. Li, S. Zhao, S. Li, Y. Ge, R. Wang, L. Zheng, J. Xu, M. Sun, Q. Jiang, Y. Zhang, H. Wei, *Small* 15 (2019) e1904486.

- [3] W. Teng, Z. Zhang, Y. Wang, Y. Ye, E. Yinwang, A. Liu, X. Zhou, J. Xu, C. Zhou, H. Sun, F. Wang, L. Zhang, C. Cheng, P. Lin, Y. Wu, Z. Gou, X. Yu, Z. Ye, *Small* 17 (2021) e2102315.
- [4] X. Hu, J. Huang, Y. Wei, H. Zhao, S. Lin, C. Hu, Z. Wang, Z. Zhao, X. Zang, *Adv. Sci.* 9 (2022) e2105499.
- [5] A. Oliva, M.C. Miele, D. Al Ismail, F. Di Timoteo, M. De Angelis, L. Rosa, A. Cutone, M. Venditti, M.T. Mascellino, P. Valenti, C.M. Mastroianni, *Front. Microbiol.* 12 (2021) 750460.
- [6] B. Li, T.J. Webster, *J. Orthop. Res.* 36 (2018) 22–32.
- [7] H.M.L. Muhlhofer, S. Feihl, C. Suren, I.G.J. Banke, F. Pohlig, R. von Eisenhart-Rothe, *Orthopade* 49 (2020) 277–286.
- [8] C.J. Cooper, T.P. Murphy, D.E. Cutlip, K. Jamerson, W. Henrich, D.M. Reid, D.J. Cohen, A.H. Matsumoto, M. Steffes, M.R. Jaff, M.R. Prince, E.F. Lewis, K.R. Tuttle, J.I. Shapiro, J.H. Rundback, J.M. Massaro, R.B. D'Agostino Sr., L.D. Dworkin, C. Investigators, *N. Engl. J. Med.* 370 (2014) 13–22.
- [9] J. Seifert, S. Apostel, M. Frank, D. Stengel, A. Ekkernkamp, *Orthopade* 39 (2010) 777–784.
- [10] P. Ziegler, D. Schlemmer, I. Flesch, S. Bahrs, U. Stoeckle, S. Werner, C. Bahrs, *J. Orthop. Surg. Res.* 12 (2017) 114.
- [11] W. Zhou, T. Bai, L. Wang, Y. Cheng, D. Xia, S. Yu, Y. Zheng, *Bioact. Mater.* 20 (2023) 64–80.
- [12] H.Q. Feng, G.M. Wang, W.H. Jin, X.M. Zhang, Y.F. Huang, A. Gao, H. Wu, G.S. Wu, P.K. Chu, *Acs Appl. Mater. Interface* 8 (2016) 9662–9673.
- [13] X.C. Huai, G.A. Rizzi, Y.F. Wang, Q.G. Qi, G. Granozzi, W.Y. Fu, Z.J. Zhang, *Nano Today* 43 (2022) 101407.
- [14] B.H. Lee, S. Park, M. Kim, A.K. Sinha, S.C. Lee, E. Jung, W.J. Chang, K.S. Lee, J.H. Kim, S.P. Cho, H. Kim, K.T. Nam, T. Hyeon, *Nat. Mater.* 18 (2019) 620–626.
- [15] T. Ito, E. Nishiuchi, G. Fukuhara, Y. Inoue, T. Mori, *Photochem. Photobiol. Sci.* 10 (2011) 1405–1414.
- [16] A. Mazare, J. Park, S. Simons, S. Mohajernia, I. Hwang, J.E. Yoo, H. Schneider, M.J. Fischer, P. Schmuki, *Acta Biomater.* 97 (2019) 681–688.
- [17] Y.L. Zhen-Kun He, Jiahui Zhao, Junjian Zhao, Zhida Gao, Yan-Yan Song, *Appl. Surf. Sci.* 613 (2023) 155974.
- [18] J. Guo, L. Yang, Z. Gao, C. Zhao, Y. Mei, Y.-Y. Song, *Acs Catal.* 10 (2020) 5949–5958.
- [19] Z. Wang, J. Li, Y. Qiao, X. Liu, Y. Zheng, Z. Li, J. Shen, Y. Zhang, S. Zhu, H. Jiang, Y. Liang, Z. Cui, P.K. Chu, S. Wu, *Adv. Fiber Mater.* (2022) 1–13.
- [20] Y. Chong, C. Ge, G. Fang, R. Wu, H. Zhang, Z. Chai, C. Chen, J.J. Yin, *Environ. Sci. Technol.* 51 (2017) 10154–10161.
- [21] G. Wang, W. Jin, A.M. Qasim, A. Gao, X. Peng, W. Li, H. Feng, P.K. Chu, *Biomaterials* 124 (2017) 25–34.
- [22] N. Gong, X. Ma, X. Ye, Q. Zhou, X. Chen, X. Tan, S. Yao, S. Huo, T. Zhang, S. Chen, X. Teng, X. Hu, J. Yu, Y. Gan, H. Jiang, J. Li, X.J. Liang, *Nat. Nanotechnol.* 14 (2019) 379–387.
- [23] D. Wang, J. Tan, H. Zhu, Y. Mei, X. Liu, *Adv. Sci.* 8 (2021) e2004393.
- [24] M.S. Stietz, C. Lopez, O. Osifo, M.E. Tolmasky, S.T. Cardona, *Can. J. Microbiol.* 63 (2017) 857–863.
- [25] H. Cao, Y. Qiao, X. Liu, T. Lu, T. Cui, F. Meng, P.K. Chu, *Acta Biomater.* 9 (2013) 5100–5110.
- [26] S. Panda, T.K. Rout, A.D. Prusty, P.M. Ajayan, S. Nayak, *Adv. Mater.* 30 (2018) 1702149.
- [27] J. Fu, W. Zhu, X. Liu, C. Liang, Y. Zheng, Z. Li, Y. Liang, D. Zheng, S. Zhu, Z. Cui, S. Wu, *Nat. Commun.* 12 (2021) 6907.
- [28] H.H. Zirui Wang, Junjian Zhao, Xiaoxia Jian, Changyong Liu, Zhida Gao Supervision, Yan-Yan Song, *Appl. Surf. Sci.* 611 (2023) 155660.
- [29] T. Shi, X. Hou, S. Guo, L. Zhang, C. Wei, T. Peng, X. Hu, *Nat. Commun.* 12 (2021) 493.
- [30] H. Li, X. Wang, X. Zhao, G. Li, F. Pei, H. Zhang, Y. Tan, F. Chen, *Small* 16 (2020) e2004677.
- [31] L. Wang, F. Gao, A. Wang, X. Chen, H. Li, X. Zhang, H. Zheng, R. Ji, B. Li, X. Yu, J. Liu, Z. Gu, F. Chen, C. Chen, *Adv. Mater.* 32 (2020) e2005423.
- [32] K. Du, G.H. Liu, X.Y. Chen, K.Y. Wang, *Electro Acta* 277 (2018) 244–254.
- [33] W. Zhao, I.W. Chen, F.Q. Huang, *Nano Today* 27 (2019) 11–27.
- [34] J.B. Xue, S. Jiang, C.K. Lei, H. Chang, J.Q. Gao, X.G. Liu, Q. Li, Q.Q. Shen, *Nano Res.* (2022) 2259–2270.
- [35] B. Santara, P.K. Giri, K. Imakita, M. Fujii, *Nanoscale* 5 (2013) 5476–5488.
- [36] T. Wu, H. Zhao, X. Zhu, Z. Xing, Q. Liu, T. Liu, S. Gao, S. Lu, G. Chen, A.M. Asiri, Y. Zhang, X. Sun, *Adv. Mater.* 32 (2020) e2000299.
- [37] Z.X. Sun, K. Sun, M.L. Gao, O. Metin, H.L. Jiang, *Angew. Chem. Int. Ed.* 61 (2022) e202206108.
- [38] D.K. Pallotti, L. Passoni, F. Gesuele, P. Maddalena, F. Di Fonzo, S. Lettieri, *ACS Sensors* 2 (2017) 61–68.
- [39] J.M. Cho, M.H. Sun, T.H. Kim, S.J. Cho, *J. Nanosci. Nanotechnol.* 10 (2010) 3336–3340.
- [40] T. Thajudheen, A.G. Dixon, S. Gardonio, I. Arcon, M. Valant, *J. Phys. Chem. C Nanomater Interfaces* 124 (2020) 19929–19936.
- [41] J.F. Lingling Yang, Jia-Ning Wang, Zhida Gao, Jingwen Xu, Ye Mei, Yan-Yan Song, *Chin. Chem. Lett.* 33 (2022) 5169–5173.
- [42] N.A. Deskins, G.A. Kimmel, N.G. Petrik, *J. Phys. Chem. Lett.* 11 (2020) 9289–9297.
- [43] I.M. Nadeem, G.T. Harrison, A. Wilson, C.L. Pang, J. Zegenhagen, G. Thornton, *J. Phys. Chem. B* 122 (2018) 834–839.
- [44] N.J. Dodd, A.N. Jha, *Photochem. Photobiol.* 87 (2011) 632–640.
- [45] G. Liu, T. Zhang, T. Wang, H. Yamashita, Y. Zhao, X. Qian, *Appl. Catal. B: Environ.* 296 (2021) 120370.
- [46] V.R.I. Kaila, M. Wikstrom, *Nat. Rev. Microbiol.* 19 (2021) 319–330.
- [47] S.H. Light, R. Meheust, J.L. Ferrell, J. Cho, D. Deng, M. Agostoni, A.T. Iavarone, J.F. Banfield, S.E.F. D'Orazio, D.A. Portnoy, *Proc. Natl. Acad. Sci. USA* 116 (2019) 26892–26899.
- [48] Q. Gao, Z. Wang, Y. Rao, Y. Zhao, J. Cao, K.F. Ho, Y. Zhai, M. Xiong, J. Li, Y. Huang, *J. Hazard. Mater.* 443 (2023) 130275.
- [49] Q. Liu, Y. Wu, J. Li, E. Liu, F. Tian, H. Zhao, R. Chen, *J. Inorg. Biochem.* 231 (2022) 111778.
- [50] B. Shao, J. Zhang, J. Huang, B. Qiao, Y. Su, S. Miao, Y. Zhou, D. Li, W. Huang, W. Shen, *Small Methods* 2 (2018) 1800273.
- [51] T. Wu, W. Kong, Y. Zhang, Z. Xing, J. Zhao, T. Wang, X. Shi, Y. Luo, X. Sun, *Small Methods* 3 (2019) 1900356.